

AUTHOR QUERY FORM

	<p>Journal: J. Appl. Phys. Article Number: JAP24-AR-05791</p>	<p>Please provide your responses and any corrections by annotating this PDF and uploading it to AIP's eProof website as detailed in the Welcome email.</p>
---	---	--

Dear Author,

Below are the queries associated with your article; please answer all of these queries before sending the proof back to AIP.

Article checklist: In order to ensure greater accuracy, please check the following and make all necessary corrections before returning your proof.

1. Is the title of your article accurate and spelled correctly?
2. Please check affiliations including spelling, completeness, and correct linking to authors.
3. Did you remember to include acknowledgment of funding, if required, and is it accurate?

Location in article	Query / Remark: click on the Q link to navigate to the appropriate spot in the proof. There, insert your comments as a PDF annotation.
Q1	Please check that the author names are in the proper order and spelled correctly. Also, please ensure that each author's given and surnames have been correctly identified (given names are highlighted in red and surnames appear in blue).
Q2	Please provide city for affil 1.
Q3	Please reword the sentence beginning with "Because $k_1\dots$ " so that your meaning will be clear to the reader.
Q4	In the sentence beginning "The sample is..." please verify that "previous subsection" refers to Subsection III
	<p>Please confirm ORCIDs are accurate. If you wish to add an ORCID for any author that does not have one, you may do so now. For more information on ORCID, see https://orcid.org/.</p> <p>Mathieu Maréchal–0009-0009-8496-5750 Alan Geslain Jean-Philippe –0000-0002-9308-8261 Vicente Romero-García–0000-0002-3798-6454 Olivier Dazel–0000-0002-0534-000X</p>
	<p>Please check and confirm the Funder(s) and Grant Reference Number(s) provided with your submission:</p> <p></p> <p>Please add any additional funding sources not stated above:</p>

Thank you for your assistance.

¹ A general spectral collocation method for ² computing the dispersion relations of guided ³ acoustic waves in multilayer dissipative structures

⁴⁵ Cite as: J. Appl. Phys. **137**, 000000 (2025); doi: [10.1063/5.0242405](https://doi.org/10.1063/5.0242405)⁶ Submitted: 4 October 2024 · Accepted: 13 February 2025 ·⁷ Published Online: ■■■ 2025

Q1

⁸ **Mathieu Maréchal**,^{1,a)} **Alan Geslain**,¹ **Jean-Philippe Groby**,¹ **Vicente Romero-García**,² and **Olivier Dazel**¹ ⁹ AFFILIATIONS¹⁰ ¹Laboratoire d'Acoustique de l'Université du Mans (LAUM), UMR 6613, Institut d'Acoustique—Graduate School (IA-GS), CNRS,
¹¹ Le Mans Université, ■, France¹² ²Instituto Universitario de Matemática Pura y Aplicada (IUMPA), Universitat Politècnica de Valencia, Camino de Vera s/n,
¹³ 46022 Valencia, Spain¹⁴¹⁵ ^{a)}Author to whom correspondence should be addressed: mathieu.marechal@univ-lemans.fr¹⁶¹⁷ ABSTRACT

¹⁸ A spectral collocation method is proposed to compute the complex wavenumber–real frequency dispersion relations of guided acoustic
¹⁹ waves in multilayer structures involving dissipative materials. The nature of these dissipative materials is initially considered to be arbitrary,
²⁰ i.e., poroelastic, viscoelastic, or viscoacoustic. For a given frequency, the complex wavenumbers as well as the physical fields, which are
²¹ further used to evaluate the Poynting vectors and analyze the energy flux, are obtained by solving a generalized eigenvalue problem. The
²² latter arises from a set of discretized equations of motion and appropriate boundary (coupling) conditions. These equations of motion and
²³ boundary (coupling) conditions are imposed by the nature of the material composing each layer of the structure. A focus is made on
²⁴ poroelastic layers. The dispersion relation of a two-layer elastic–poroelastic structure is analyzed, as well as the energy flows in the structure.
²⁵ The results as calculated with the present spectral collocation method are validated against those obtained with a classical complex
²⁶ root-finding (Müller) method and experiments.

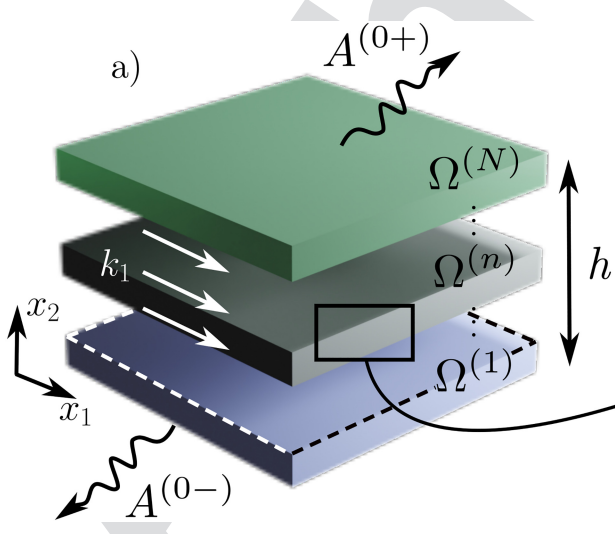
²⁷ © 2025 Author(s). All article content, except where otherwise noted, is licensed under a Creative Commons Attribution (CC BY) license
²⁸ (<https://creativecommons.org/licenses/by/4.0/>). <https://doi.org/10.1063/5.0242405>²⁹ I. INTRODUCTION

³⁰ Dealing with guided acoustic waves in multilayer structures of
³¹ dissipative (viscoelastic, viscothermal, or poroelastic) material requires
³² the evaluation of complex wavenumber–real frequency dispersion
³³ relations. Solving for these dispersion relations consists of finding
³⁴ complex roots of complex characteristic equations, which often arise
³⁵ from complex matrix determinants and can rarely be solved analyti-
³⁶ cally. Various methods,^{1,2} among which the Müller algorithm,³ are
³⁷ commonly used to achieve this challenging task. These methods
³⁸ usually rely on preliminary semi-analytical derivations, require multi-
³⁹ ple initial guesses, and are iterative so that they can get stuck in local
⁴⁰ minima. Computing the complex wavenumber–real frequency disper-
⁴¹ sion relation in a reliable and robust way is, thus, of primary

importance. Commercial software, such as Disperse,⁴ or open-source software, such as Dispersion Calculator,^{5,6} is available for calculating dispersion curves. They use mode tracing or root-finding methods and focus mainly on multilayer elastic structures. Alternatively, several numerical methods can be used, such as the finite element method,⁷ the Semi-Analytical Finite Element method (SAFE),^{8–10} or spectral methods.¹¹ Spectral methods are especially relevant in this framework. They are numerical approximation techniques that seek the solution of a differential equation using a finite series of infinitely differentiable basis functions with *spectral accuracy*.¹²

The propagation and dispersion of waves in multilayer systems have long been investigated.^{13,14} Spectral methods have been developed to cope with wave radiation problems but have also

emerged in the last few decades to solve dispersion relations.¹⁵ Effectively, the numerical scheme boils down to discretizing the geometry along the layer thickness and solving an eigenvalue problem. Here, a collocation method is used to discretize the geometry. A finite-dimension polynomial basis is chosen, and the collocation points are distributed according to the roots of this polynomial basis. Leaky modes appear in practice when multilayer structures are surrounded by one or two half-spaces. Accounting for this phenomenon brings us closer to practical considerations regarding these systems, as they would radiate part of the acoustic energy back to the surrounding medium, although it adds hardships to the modeling of the system; the waves modeled in these half-spaces should satisfy some radiation condition. These can be imposed by implementing perfectly matched layers,¹⁶ by using a bounded mapping, and applying a Spectral Collocation Method (SCM) to all layers of the extended system,¹⁷ or by using a suitable change of variable and solving a non-linear eigenvalue problem.¹⁸ This last method inspires the current work. We propose a SCM suitable for solving complex wavenumber-real frequency dispersion relations in multilayer systems involving dissipative media. As a way of example, we will focus on multilayer poroelastic systems. Mechanical wave propagation in bulk poroelastic materials is well understood and modeled thanks to the seminal contributions of Biot^{19–22} and subsequent contributions, notably by Johnson *et al.*²³ and Allard *et al.*^{24,25} concerning the modeling of viscothermal losses. Although poroelastic materials are bounded in practice and are usually encapsulated in more complex multilayer structures combining layers of materials of different nature in geophysics and acoustics, there are only a few studies on the dispersion relation of guided acoustic waves in poroelastic,^{26–28} porous,^{29,30} or anisotropic poroelastic layers.³¹ The SCM has already been used to solve the dispersion relation of guided acoustic waves in elastic layered rings^{32,33} or anisotropic elastic multilayer systems³⁴ but has never been used to cope with multilayer systems involving dissipative materials of arbitrary nature.



This work aims at filling this gap and is divided into two sections. First, the SCM is derived for generic multilayer configurations possibly coupled to two surrounding identical fluid half-spaces. A two-layer elastic-poroelastic structure is then considered by way of an example. The dispersion relation computed with the SCM method is compared to that obtained with a classical root-finding (Müller) method and that measured. The energy flow is further analyzed for this two-layer configuration, with very little additional computational cost. In Sec. III, we experimentally analyze the two-layer structure by retrieving its complex dispersion relation from displacement measurements using the SLaTCoW (Spatial LAplace Transform for COmplex Wavenumber recovery). The previously obtained numerical results can, thus, be correlated with the data of the dispersion relation.

II. SOLVING THE DISPERSION RELATIONS FOR MULTILAYER STRUCTURES

A. Spectral collocation method

Figure 1(a) depicts the general geometry of the multilayer structure considered in this article. It is composed of N homogeneous layers of arbitrary nature. The n th layer has a thickness of $h^{(n)}$ and occupies the domain $\Omega^{(n)}$. The lower and upper interfaces are denoted as $\Gamma^{(n-1)}$ and $\Gamma^{(n)}$. The multilayer structure is assumed to be two-dimensional, of infinite extent along x_1 , and bounded along the x_2 -axis between 0 and the total structure thickness $h = \sum_{n=1}^N h^{(n)}$. Outgoing waves radiate above and below the structure in two fluid half-spaces $\Omega^{(0\pm)}$, occupied by the same fluid.

We assume an implicit time dependence $e^{-i\omega t}$. The physical fields associated with the guided waves in the n th layer propagating along the positive x_1 axis take the form

$$\Theta^{(n)}(\mathbf{x}) = s^{(n)}(k_1, x_2) e^{ik_1 x_1}, \quad (1)$$

where $s^{(n)}(k_1, x_2)$ is the spatial Laplace transform of $\Theta^{(n)}(\mathbf{x})$ and k_1 is the complex-valued x_1 -component of the wavenumber. Note that

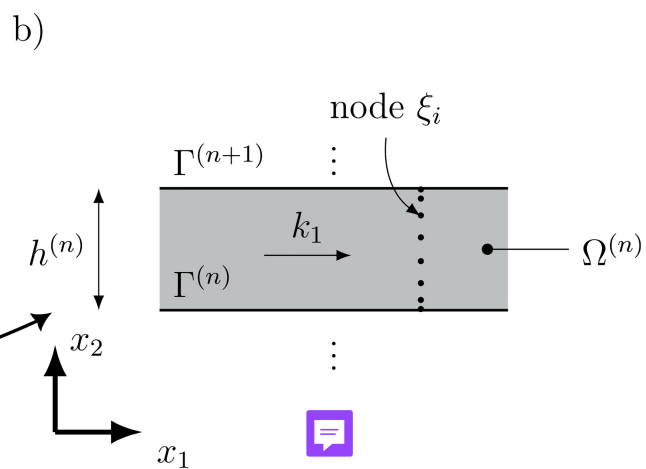


FIG. 1. (a) Sketch of the geometry of the multilayer system and (b) zoom on the n th layer.

120 the spatial Laplace transform is used instead of the spatial Fourier
121 transform because k_1 is complex-valued. Because k_1 , the x_1 component
122 of the wavenumber is complex-valued. The physical fields that
123 compose $\Theta^{(n)}(\mathbf{x})$ depend on the nature of the material occupying
124 the n th layer. Introducing $\Theta^{(n)}(\mathbf{x})$ in the corresponding wave equations
125 (of second order in space in this work) reduces to a second-order
126 differential operator $\mathcal{L}^{(n)}$ in x_2 , which depends on the material properties and can further be developed as a second-order
127 polynomial in k_1 ,

$$\mathcal{L}^{(n)}(x_2)s^{(n)}(k_1, x_2) = \left(k_1^2 \mathcal{L}_2^{(n)}(x_2) + k_1 \mathcal{L}_1^{(n)}(x_2) + \mathcal{L}_0^{(n)}(x_2) \right) s^{(n)}(k_1, x_2) = \mathbf{0}, \quad (2)$$

129 where $\mathcal{L}_j^{(n)}$ are the coefficients of the polynomial expansion

130 $j = 0, 1, 2$. Please note that this operator is nothing but the spatial
131 Laplace transform of the equations of motion.

The interface (boundary) conditions at $\Gamma^{(n)}$ between the 132
133 $n+1$ th and the n th layers again depend on the nature of these two
134 layers but can be formally written in the form

$$\mathcal{C}^{(n)-}s^{(n)}(k_1)|_{\Gamma^{(n)}} - \mathcal{C}^{(n)+}s^{(n+1)}(k_1)|_{\Gamma^{(n)}} = \mathbf{0}, \quad (3)$$

where $\mathcal{C}^{(n)\pm}$ are interfaces operators, which involve differential 135
136 operators of maximum second-order in x_2 . Following this procedure 137
138 and introducing $\mathbf{S} = (s^{(0-)} \dots s^{(n)} \dots s^{(0+)})^T$, with T denoting 139
140 transposition, the problem can be cast in a matrix form, whose coefficients are differential operators in x_2 ,

$$KS(k_1, x_2) = \begin{pmatrix} \mathcal{C}^{(0-)} & -\mathcal{C}^{(0+)} & 0 \\ 0 & \mathcal{L}^{(1)}(x_2) & 0 \\ 0 & \mathcal{C}^{(1-)} & -\mathcal{C}^{(1+)} \\ 0 & \mathcal{L}^{(2)}(x_2) & 0 \\ \vdots & \vdots & \vdots \\ 0 & \mathcal{L}^{(N)}(x_2) & 0 \\ 0 & \mathcal{C}^{(N-)} & -\mathcal{C}^{(N+)} \end{pmatrix} S(k_1, x_2) = \mathbf{0}. \quad (4)$$

142 to the power order k_1 . Index $1'$ corresponds to the term in $k_2^{(0)}$. 161
143 Introducing Eqs. (2) and (6) in Eq. (4) leads to 162

$$(k_1^2 K_2 + k_1 K_1 + K_0 + ik_2^{(0)} K_{1'}) \mathbf{S} = \mathbf{0}. \quad (7)$$

This eigenvalue problem is non-linear because of the presence 163
164 of the term $k_2^{(0)}$. Making use of the following changes of variable 165
166 $k_1 = k^{(0)}(\gamma + \gamma^{-1})/2$ and $k_2^{(0)} = k^{(0)}(\gamma - \gamma^{-1})/2i$ ^{35,36} and companion linearization,³⁷ a generalized eigenvalue problem is formed 167
168 and solved for γ , from which the dispersion relation can be calculated. More details on this procedure can be found in.¹⁸ Note that 169
170 the first or the last column of Eq. (4) vanishes when radiation is 171
172 absent on either side of the multilayer system. The situation is 173
174 different when both fluid half-spaces disappear. The eigenvalue 175
176 problem Eq. (7) is no longer non-linear and the problem can 177
178 directly be solved after companion linearization. Note also that 179
180 fluid half-spaces are only considered for the sake of simplicity and 181
182 that this procedure can be adapted to any kind of material occupying 183
184 the half-spaces, as described recently.³⁸ Note finally that this 185
186 procedure avoids discretization of these two half-spaces. 187

To numerically solve the problem, the spatial Laplace transform of the physical fields in each n -th layer are expanded as 188

$$s^{(n)}(x_2) \approx \underline{s}^{(n)}(x_2) = \sum_{m=0}^M \alpha_m^{(n)} \underline{\psi}_m(\xi^{(n)}), \quad (8)$$

where α_m are coefficients of the polynomial expansion, $\underline{\psi}_m$ are the 189

160 with the subscript denoting the submatrices rearranged according

181 Chebyshev polynomial of order m , and $\xi^{(n)} = 2(x_2 - \sum_{j=1}^{n-1} h^{(j)})$
 182 $/h^{(n)} - 1$, $\in [-1, 1]$. Underlined variables represent discrete
 183 vectors and double-underlined variables discrete matrices. The goal
 184 of this approximation is to discretize the differential operators
 185 in x_2 appearing in the problem. To do so, the SCM is employed.
 186 $\xi_j^{(n)}$ is discretized on the roots of the Chebyshev polynomials,
 187 $\xi_j^{(n)} = \cos\left(\frac{j\pi}{M^{(n)}}\right)$ with $j = 0 \dots M^{(n)}$. Please note that $\xi_j^{(n)}$ discretely
 188 runs from 1 to -1 with increasing j , while $\xi^{(n)}$ continuously runs
 189 over the same interval but in the opposite direction, i.e., from -1
 190 to 1. These collocation points/nodes form a non-uniform grid
 191 along the thickness of each layer. This discretization is usually pre-
 192 ferred because the collocation points are clustered at the inter-
 193 faces.¹² The locations of these nodes are presented in Fig. 1(b) for
 194 the n -th layer with an arbitrary value $M^{(n)} = 8$. The differential
 195 operators in the n -th layer are thus represented by differentiation
 196 matrices (DMs), such that

$$\begin{aligned} s^{(n)}(x_2) &\rightarrow \underline{\underline{L}} \cdot \underline{\underline{s}}^{(n)}(\xi_j), \quad \partial_2 s^{(n)}(x_2) \rightarrow \left(\frac{2}{h^{(n)}}\right) \underline{\underline{D}}_2 \cdot \underline{\underline{s}}^{(n)}(\xi_j) = \underline{\underline{D}}_2^{(n)} \cdot \underline{\underline{s}}^{(n)}(\xi_j), \\ \partial_{22} s^{(n)}(\xi_j) &\rightarrow \left(\frac{2}{h^{(n)}}\right)^2 \underline{\underline{D}}_{22} \cdot \underline{\underline{s}}^{(n)}(\xi_j) = \underline{\underline{D}}_{22}^{(n)} \cdot \underline{\underline{s}}^{(n)}(\xi_j). \end{aligned} \quad (9)$$

197 where $\underline{\underline{L}}$ is the identity matrix and $\underline{\underline{D}}_2$ and $\underline{\underline{D}}_{22}$ are respectively the
 198 first-order and second-order normalized DMs. Contrary to an
 199 interpolation with Chebyshev polynomials, DMs interpolate the
 200 functions and their spatial derivatives directly and thus do not
 201 involve the polynomial expansion coefficients per se.³⁹ Note that
 202 the normalized DMs are denoted as $\underline{\underline{D}}_2^{(n)}$ and $\underline{\underline{D}}_{22}^{(n)}$ in the following.
 203 These matrices are square and have a size of $(M \times M)$. This size
 204 also directly depends on the order of the considered Chebyshev
 205 polynomials. The formulation prevents the occurrence of roundoff
 206 errors, which is of particular importance when SCM is applied to
 207 solve eigenvalue problems.⁴⁰

208 The linear operator $\mathcal{L}^{(n)}$ is discretized as a matrix $\underline{\underline{L}}^{(n)}$ with
 209 size $(P^{(n)}(M^{(n)} - 1), P^{(n)}(M^{(n)} + 1))$, where $P^{(n)}$ is the number of
 210 physical fields required to describe the wave propagation in the
 211 layer and again depends on the nature of the material this layer is
 212 composed of. The first and the last rows of the DMs are removed
 213 because they are used to apply the interface conditions at $\Gamma^{(n+1)}$
 214 and $\Gamma^{(n)}$ respectively. The interface operators $\mathcal{C}^{(n)\pm}$ are effectively
 215 expressed in terms of this first row of the DMs of the n -th layer
 216 and this last row of the DMs of the $(n+1)$ -th layer. These rows
 217 respectively correspond to the first, i.e., $\xi_{M^{(n)}} = -1$ and $\xi^{(n)} = 1$,
 218 and last collocation nodes of the n -th and $(n+1)$ -th layers, i.e.,
 219 $\xi_0 = 1$ and $\xi^{(n+1)} = -1$. These vectors are subsequently denoted
 220 $\underline{\underline{I}}^{(n+1)-}$, $\underline{\underline{I}}^{(n)+}$, $\underline{\underline{D}}_2^{(n+1)-}$, $\underline{\underline{D}}_2^{(n)+}$, $\underline{\underline{D}}_{22}^{(n+1)-}$, and $\underline{\underline{D}}_{22}^{(n)+}$. The interface
 221 matrix $\underline{\underline{C}}^{(n)-}$ is of size $(P^{(n)} + P^{(n+1)}, P^{(n)}(M^{(n)} + 1))$ and the inter-
 222 face matrix $\underline{\underline{C}}^{(n)+}$ is of size $(P^{(n)} + P^{(n+1)}, P^{(n+1)}(M^{(n+1)} + 1))$.

223 Finally, the full $(\sum_{n=0}^N M^{(n)} P^{(n)} + 2, \sum_{n=0}^N M^{(n)} P^{(n)} + 2)$ -matrix
 224 system for the general multilayer system is

$$\underline{\underline{K}} \cdot \underline{\underline{S}} = \begin{pmatrix} \underline{\underline{C}}^{(0-)} & -\underline{\underline{C}}^{(0+)} & 0 & & & \\ 0 & \underline{\underline{L}}^{(1)} & 0 & & & \\ 0 & \underline{\underline{C}}^{(1-)} & -\underline{\underline{C}}^{(1+)} & 0 & & \\ 0 & \underline{\underline{L}}^{(2)} & 0 & & & \\ & \ddots & \ddots & \ddots & & \\ 0 & \underline{\underline{L}}^{(N)} & 0 & & & \\ 0 & \underline{\underline{C}}^{(N-)} & -\underline{\underline{C}}^{(N+)} & 0 & & \end{pmatrix} \times \begin{pmatrix} A^{(0-)} \\ \underline{\underline{s}}^{(1)} \\ \underline{\underline{s}}^{(2)} \\ \vdots \\ \underline{\underline{s}}^{(N)} \\ A^{(0+)} \end{pmatrix} = 0. \quad (10)$$

225 This system is cast in the form of a generalized eigenvalue
 226 problem that is solved by traditional eigenvalue solvers at each fre-
 227 quency. The dispersion relation for the acoustic guided wave in the
 228 dissipative multilayer system is calculated, repeating the procedure
 229 for each frequency ω .
 230

B. Solving the dispersion relation with the Müller 232 algorithm

233 The dispersion relation of a multi-layer dissipative structure is
 234 more commonly calculated with a secant-based algorithm as the
 235 Müller algorithm. The latter relies on a semi-analytic description of
 236 the fields. These fields are best written in each layer, independently
 237 of the nature of the material it is composed of, using the potentials,
 238 i.e., decomposing the field $\boldsymbol{\theta} = \nabla\varphi + \nabla \times \boldsymbol{\psi}$ into an irrotational
 239 component φ and a transverse component $\boldsymbol{\psi} = \psi \mathbf{e}_3$. The spatial
 240 Laplace transform of the potentials in the n th layer is entirely
 241 described by
 242

$$\tilde{\boldsymbol{\theta}}_n(k_1, x_2) = A_X^{(n)+} e^{ik_{2,X}^{(n)}(x_2 - h^{(n)})} + A_X^{(n)-} e^{-ik_{2,X}^{(n)}(x_2 - h^{(n)})}, \quad (11)$$

243 with $A_X^{(n)\pm}$ the up- and down-going wave amplitudes,
 244 $k_{2,X}^{(n)} = \sqrt{(k_X^{(n)})^2 - k_1^2}$, such that $\text{Re}(k_{2,X}^{(n)}) \geq 0$, and X refers to the
 245 type of wave, i.e., shear, compressional, or acoustic. If necessary,
 246 these Laplace transform representations are complemented by
 247 those of the pressure field in the fluid half-spaces provided in
 248 Eq. (5).

249 The boundary conditions are applied at each interface, and
 250 the set of equations is cast into the following matrix form
 251 $\mathbf{M}(k_1)\mathbf{q} = 0$, with \mathbf{q} a vector containing the amplitudes of each
 252 field/potential. The modes of the system correspond to the wave-
 253 numbers k_1 for which the matrix $\mathbf{M}(k_1)$ is singular; i.e.,

$$\det(\mathbf{M}(k_1)) = 0. \quad (12)$$

254 These wavenumbers are the complex roots of an implicit complex-
 255 valued equation. They are evaluated by running our own

implementation of the Müller algorithm³ from three initial guesses. This equation is solved iteratively for each frequency ω , giving the dispersion relation.

In addition, \mathbf{q} can be obtained by computing the nullspace of \mathbf{M} .⁴¹ (This null space is computed using singular value decomposition as embedded in the `linalg.null_space` function from the

Python package SciPy.) The amplitudes of the potentials in the layers are thus evaluated, enabling all the physical fields that depend on these potentials to be calculated. However, the \mathbf{M} matrix becomes increasingly tedious to write as the number of layers increases, and even more so when it comes to calculating the roots of its determinant and nullspaces. Nevertheless, this

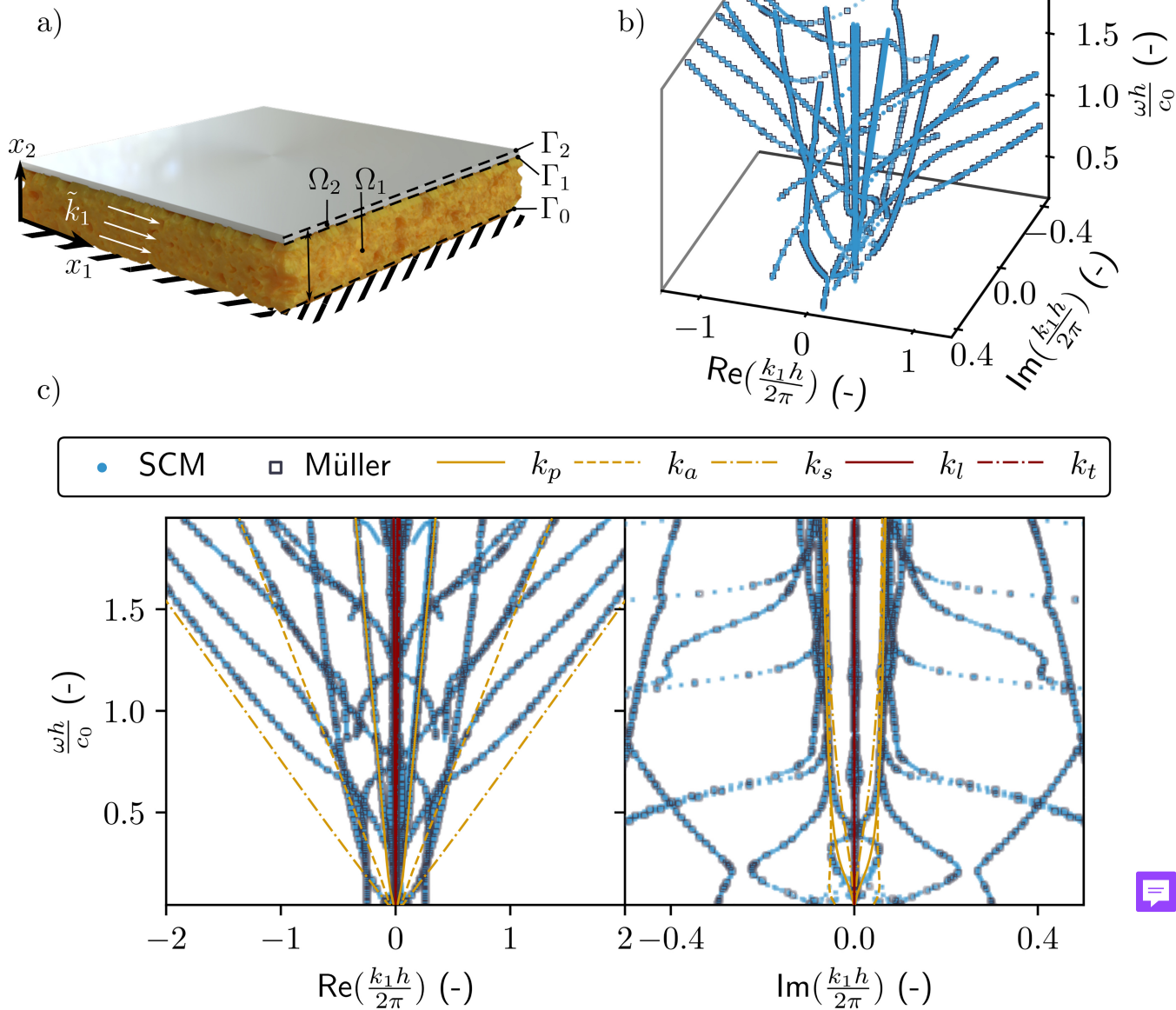


FIG. 2. (a) Sketch of the two-layer structure geometry. (b) 3D view of the complex wavenumber–real frequency dispersion relation and (c) real and imaginary parts of the dispersion relation. Blue dots represent the results as calculated with the SCM, and black open markers represent those as calculated with the Müller method. Bulk wave-numbers in the poroelastic and elastic materials are highlighted in yellow and dark red, respectively.

approach remains a fairly effective way of providing a reference solution for validating numerical results when studying a two-layer system.

III. APPLICATION TO A TWO-LAYER POROELASTIC-ELASTIC STRUCTURE

In this section, the calculation of the dispersion relation for guided waves in a two-layer structure, i.e., $N = 2$, is used as an example of the application of the present SCM. This two-layer structure consists of a $h^{(1)}$ -thick poroelastic layer, coated on one side by a $h^{(2)}$ -thick aluminum plate, that is radiating in a fluid half-space, and rigidly backed on the other side as depicted in Fig. 2(a). The SCM results are analyzed and compared to those obtained with the Müller root-finding method.

A. Numerical scheme

The pressure field $p^{(1)}$ and the two components of the frame displacement, $u_{1,s}^{(1)}$ and $u_{2,s}^{(1)}$, i.e., $P^{(1)} = 3$, as well as the two components of the elastic displacement, $u_1^{(2)}$ and $u_2^{(2)}$, i.e., $P^{(2)} = 2$, are used to model the propagation in the poroelastic and in the elastic layers, respectively. The $\{\mathbf{u}_s, p\}$ formulation is used⁴² for the poroelastic medium. The more usual displacement formulations ($\{\mathbf{u}_s, \mathbf{u}_f\}$ ¹⁹ or $\{\mathbf{u}_s, \mathbf{w}\}$ ²¹) cannot be used in the present case, because the number of physical fields they rely on, i.e., 2 , is different from that of the potentials in the layer, i.e., 3 .

In total, five physical fields in the two-layer structure and an additional amplitude for the acoustic wave radiated toward $x_2 \rightarrow \infty$ are needed to solve for the dispersion relation. Each domain is discretized on $M^{(j)}$, $j = 1, 2$, collocation points.

In more detail, the $\{\mathbf{u}_s, p\}$ formulation of the Biot theory⁴² is employed to model the propagation in the homogeneous isotropic poroelastic layer. The coupled equations of motion read as

$$\begin{cases} \nabla \cdot \hat{\boldsymbol{\sigma}}_s^{(1)} + \hat{\rho}\omega^2 \mathbf{u}_s^{(1)} + \beta \nabla p^{(1)} = 0, \\ \frac{\nabla^2 p^{(1)}}{\rho_{22}\omega^2} - \frac{\beta}{\phi^2} \nabla \cdot \mathbf{u}_s^{(1)} + \frac{1}{R} p^{(1)} = 0, \end{cases} \quad (13)$$

where $\hat{\boldsymbol{\sigma}}_s^{(1)} = \hat{A} \nabla \cdot \mathbf{u}_s^{(1)} \mathbf{I} + 2N_s \boldsymbol{\varepsilon}_s$ is the *in vacuo* solid stress tensor, with $\boldsymbol{\varepsilon}_s$, the solid-phase strain tensor. The parameters are generally expressed in terms of the elastic coefficients P , Q , and R and the effective densities ρ_{11} , ρ_{12} , and ρ_{22} initially introduced by Biot^{19,43} as

$$\hat{A} = P - 2N_s - \frac{Q^2}{R}, \quad \hat{\rho} = \rho_{11} - \frac{\rho_{12}^2}{\rho_{22}}, \quad \beta = \phi \left(\frac{\rho_{12}}{\rho_{22}} - \frac{Q}{R} \right). \quad (14)$$

These parameters depend on the frame properties and on the effective density $\rho_{eq}(\omega)$ and bulk modulus $K_{eq}(\omega)$ of the fluid phase as reminded in Appendix A. In short, a poroelastic material is entirely described by the porosity ϕ , the shear modulus of the frame N_s , the Poisson ratio ν , the density of the frame ρ_1 , the viscous and thermal characteristic lengths Λ and Λ' , tortuosity α_∞ , and the flow resistivity R_f when saturated by a light fluid.^{19,23,24} All these parameters are real valued except for the shear modulus, which incorporates a viscoelastic damping factor.

Introducing $\tilde{\mathbf{s}}^{(1)} = (\tilde{u}_1^s, \tilde{u}_2^s, \tilde{p})^T$, the spatial Laplace transform of Eq. (13) is expanded in the form of Eq. (2) with

$$\begin{aligned} \mathcal{L}_0^{(1)} &= \begin{pmatrix} N_s \partial_{22} + \hat{\rho}\omega^2 & 0 & 0 \\ 0 & \hat{P}\partial_{22} + \hat{\rho}\omega^2 & \beta\partial_2 \\ 0 & -\beta/\phi^2\partial_2 & 1/R + \partial_{22}/(\rho_{22}\omega^2) \end{pmatrix}, \\ \mathcal{L}_1^{(1)} &= \begin{pmatrix} 0 & i\hat{P}\partial_2 & i\beta \\ i(\hat{A} + N_s)\partial_2 & 0 & 0 \\ -i\beta/\phi^2 & 0 & 0 \end{pmatrix}, \text{ and } \mathcal{L}_2^{(1)} = \begin{pmatrix} \hat{P} & 0 & 0 \\ 0 & N_s & 0 \\ 0 & 0 & 1/(\rho_{22}\omega^2) \end{pmatrix}. \end{aligned} \quad (15)$$

Finally, the discretized equations of motion read as

$$\begin{aligned} \underline{\underline{L}}^{(1)} \underline{\underline{s}}^{(1)} &= \begin{pmatrix} (\omega^2 \hat{\rho} - k_1^2 \hat{P}) \underline{\underline{I}} + N_s \underline{\underline{D}}_{22} & ik_1(\hat{P} - N_s) \underline{\underline{D}}_{22} & -ik_1 \beta \underline{\underline{I}} \\ ik_1(\hat{P} - N_s) \underline{\underline{D}}_2 & \hat{P} \underline{\underline{D}}_{22} + (\omega^2 \hat{\rho} - k_1^2 N_s) \underline{\underline{I}} & \beta \underline{\underline{D}}_2 \\ -i\beta \omega^2 \underline{\underline{I}} & -\beta \omega^2 \underline{\underline{D}}_2 & \frac{k_1^2}{\phi^2} \underline{\underline{I}} + \frac{\omega^2}{R} \underline{\underline{I}} \end{pmatrix} \underline{\underline{s}}^{(1)} \\ &= 0. \end{aligned} \quad (16)$$

The equation of motion in the elastic medium is derived from the fundamental elasticity equations⁴⁴ and reads as

$$\rho \omega^2 \mathbf{u}^{(2)} + (\lambda + \mu) \nabla(\nabla \cdot \mathbf{u}^{(2)}) + \mu \nabla^2 \mathbf{u}^{(2)} = 0, \quad (17)$$

where ρ is the density and λ and μ are the Lamé coefficients. The corresponding discretized equation of motion is

$$\underline{\underline{L}}^{(2)} \underline{\underline{s}}^{(2)} = \left(\frac{\rho^{(2)}}{\mu} \omega^2 \underline{\underline{I}} + \begin{pmatrix} -k_1^2(\lambda/\mu + 2) \underline{\underline{I}} + \underline{\underline{D}}_{22} & ik_1(\lambda/\mu + 1) \underline{\underline{D}}_2 \\ ik_1(\lambda/\mu + 1) \underline{\underline{D}}_2 & (\lambda/\mu + 2) \underline{\underline{D}}_{22} - k_1^2 \underline{\underline{I}} \end{pmatrix} \right) \underline{\underline{s}}^{(2)} = 0. \quad (18)$$

In addition, the same procedure can be followed for the equation of motion of a wave propagating in a layer of fluid material.³²¹ We give its expression in order to provide an exhaustive list of the types of layers that can be modeled using the present method. The Helmholtz equation, $(\nabla^2 + k_0^2)p = 0$, with k_0 being the bulk wave-number and p being the pressure field in the fluid material, is discretized into the form

$$(\underline{\underline{D}}_{22} - k_1^2 + k_0^2) \underline{\underline{p}} = 0. \quad (19)$$

The interface and boundary conditions depend on the vectors $\underline{\underline{I}}^\pm$, $\underline{\underline{D}}_2^\pm$, and $\underline{\underline{D}}_{22}^\pm$, which corresponds to the last (subscript $+$) and first row (subscript $-$) of the DMs. From the bottom to the top of the two-layer system, they are

- Rigid boundary condition at $\Gamma^{(0)}$, which leads to

$$\mathbf{u}^{(1)}(x_2 = 0) = 0, \quad \mathbf{u}_f^{(1)}(x_2 = 0) \cdot \mathbf{n} - \mathbf{u}_s^{(1)}(x_2 = 0) \cdot \mathbf{n} = 0, \quad (20)$$

the discretized form of which is

$$\underline{\underline{C}}^{(0)} \underline{s}^{(1)} = \begin{pmatrix} 0 & \underline{I}^+ & 0 \\ 0 & 0 & \underline{I}^+ \\ \frac{\phi}{\rho_{22}} \underline{D}_2^+ & 0 & -\left(1 + \frac{\rho_{12}}{\rho_{22}}\right) \omega^2 \underline{I}^+ \end{pmatrix} \begin{pmatrix} \underline{p}^{(1)} \\ \underline{u}_1^{(1)} \\ \underline{u}_2^{(1)} \end{pmatrix} = \underline{0}. \quad (21)$$

- Continuity between the poroelastic and elastic media⁴⁵ at $\Gamma^{(1)}$, which leads to

$$\boldsymbol{\sigma}^{t(1)}(x_2 = h^{(1)}) - \boldsymbol{\sigma}^{(2)}(x_2 = h^{(1)}) = 0, \quad \mathbf{u}^{(2)}(x_2 = h^{(1)}) = \mathbf{u}_s^{(1)}(x_2 = h^{(1)}), \\ \mathbf{u}_f^{(1)}(x_2 = h^{(1)}) \cdot \mathbf{n} - \mathbf{u}_s^{(1)}(x_2 = h^{(1)}) \cdot \mathbf{n} = 0, \quad (22)$$

where $\boldsymbol{\sigma}^{t(1)} = \boldsymbol{\sigma}_s - \phi(1 + Q/R)$ is the total stress tensor in the poroelastic layer. The corresponding discretized interface matrices, arising from

$$\underline{\underline{C}}^{(1)+} \underline{s}^{(2)} - \underline{\underline{C}}^{(1)-} \underline{s}^{(1)} = \underline{\underline{C}}^{(1)} \begin{pmatrix} \underline{p}^{(1)} & \underline{u}_1^{(1)} & \underline{u}_2^{(1)} & \underline{u}_1^{(2)} & \underline{u}_2^{(2)} \end{pmatrix}^T = \underline{0}, \quad (23)$$

are cast as

$$\underline{\underline{C}}^{(1)} = \begin{pmatrix} -N_s \underline{D}_2^+ & -ik_1 N_s \underline{I} & 0 & \mu \underline{D}_2^- & ik_1 \mu \underline{I}^- \\ -ik_1 \hat{A} \underline{I}^+ & -\hat{P} \underline{D}_2^+ & \phi \left(1 + \frac{Q}{R}\right) \underline{I}^+ & ik_1 \lambda \underline{I}^- & (\lambda + 2\mu) \underline{D}_2^- \\ 0 & -\underline{I}^+ & 0 & \underline{I}^- & 0 \\ 0 & 0 & -\underline{I}^+ & 0 & \underline{I}^- \\ -\phi \rho_{22} \underline{D}_2^+ & \left(1 + \frac{\rho_{12}}{\rho_{22}}\right) \omega^2 \underline{I}^+ & 0 & 0 & 0 \end{pmatrix}, \quad (24)$$

343

344

346

347 with the left-hand side corresponding to $\underline{\underline{C}}^{(1)-}$ and the right-hand side to $\underline{\underline{C}}^{(1)+}$.

- 348 • Continuity between the elastic and fluid media at $\Gamma^{(2)}$, which
349 leads to

$$\sigma_{12}^{(2)}(x_2 = h) = 0, \quad \sigma_{22}^{(2)}(x_2 = h) = -p^{(0+)}, \\ u_2^{(2)}(x_2 = h) = u_2^{(0+)}(x_2 = h). \quad (25)$$

350 The corresponding discretized interface matrix
351 $\underline{\underline{C}}^{(2)} \begin{pmatrix} \underline{u}_1^{(2)} & \underline{u}_2^{(2)} & A^{(0+)} \end{pmatrix}^T = \underline{0}$ is

$$\underline{\underline{C}}^{(2)} = \begin{pmatrix} \underline{D}_2^+ & ik_1 \underline{I}^+ & 0 \\ ik_1 \lambda \underline{I}^+ & (\lambda + 2\mu) \underline{D}_2^+ & 1 \\ 0 & \omega^2 \underline{I}^+ & ik_1 \underline{I}^+ \end{pmatrix}. \quad (26)$$

352

353 Combining the discretized interface conditions, Eqs. (21),
354 (24), and (26), with the discretized equations of motion, Eqs. (16)

355 and (18), leads to the following system:

$$\begin{pmatrix} \underline{\underline{C}}^{(0)} & 0 & 0 \\ \underline{\underline{L}}^{(1)} & 0 & 0 \\ \underline{\underline{C}}^{(1)-} & -\underline{\underline{C}}^{(1)+} & 0 \\ 0 & \underline{\underline{L}}^{(2)} & 0 \\ 0 & \underline{\underline{C}}^{(2)-} & -\underline{\underline{C}}^{(2)+} \end{pmatrix} \begin{pmatrix} \underline{s}^{(1)} \\ \underline{s}^{(2)} \\ A^{(0+)} \end{pmatrix} = \underline{0}. \quad (27)$$

This system is further expanded in the form of Eq. (7) and solved for a set of eigenvalues γ and associated eigenvectors \mathbf{S} at each frequency ω . Wavenumbers k_1 are then obtained from γ . The dispersion curve is, thus, calculated over a given frequency range. However, the condition $\text{Re}(k_2^0) \geq 0$ should be imposed to sort out the solution that do not meet it.

Although usual and simple, this two-layer structure is challenging from a numerical point of view because it involves materials with very large impedance contrasts and layers whose thicknesses differ by several orders of magnitude. These problems are partially solved by normalizing each line and rearranging the

TABLE I. Parameters of the poroelastic material (melamine foam).

Parameter (unit)	ϕ (...)	ρ_1 (kg m^{-3})	R_f (kPa s m^{-2})	Λ (μm)	Λ' (μm)	α_∞ (...)	v (...)	N_s (kPa)
Melamine	0.98	6.5	5.6	214	214	1	0.24	$11.96(1 + i0.07)$

368 terms of the matrix equation (7), leading to better numerical con-
 369 ditioning of the system.

370 B. Dispersion relation

371 The material properties of the $h^{(1)} = 52$ mm-thick poroelastic
 372 (melamine) layer are listed in Table I, while the properties of
 373 the $h^{(2)} = 1$ mm-thick aluminum plate are the density
 374 $\rho = 2700 \text{ kg m}^{-3}$ and the Lamé coefficients $\lambda = 60.75 \text{ GPa}$ and
 375 $\mu = 26.03 \text{ GPa}$. The saturating fluid and that occupying the half-
 376 space is air with density $\rho_f = 1.213 \text{ kg m}^{-3}$, the heat capacity ratio
 377 $\kappa = 1.4$, kinematic compressibility $\mu_f = 1.839 \times 10^{-5} \text{ Pa s}$, the
 378 Prandtl number $\text{Pr} = 0.71$, and adiabatic bulk modulus κP_0 , where
 379 the atmospheric pressure is $P_0 = 1.013 \times 10^5 \text{ Pa}$. The total two-
 380 layer thickness is, thus, $h = h^{(1)} + h^{(2)} = 53 \text{ mm}$. $M^{(1)} = 5$ and
 381 $M^{(2)} = 11$ collocation points are employed, respectively, in the
 382 poroelastic and elastic layers.

383 The 3D view of the complex dispersion diagram is depicted in
 384 Fig. 2(b). To ease readability, real and imaginary parts are depicted
 385 separately in Fig. 2(c). Please note that this last representation can
 386 be misleading because only the modes that lie in the complex wave-
 387 number range depicted in Fig. 2(b) are represented in Fig. 2(c).
 388 Cut-on frequencies are, thus, fictitious. The results calculated using
 389 the SCM method, plotted in blue markers, are compared with
 390 those obtained using the Müller method, plotted with black open
 391 markers. Both methods provide identical results, up to around four
 392 digits, therefore validating the present approach. Note that the
 393 SCM solutions are used as initial guesses of the Müller algorithm
 394 to shorten computational time. In this way, fewer iterations are
 395 needed for the results of the root-finding method to converge. The
 396 main advantages of SCM are that no initial guesses are needed, i.e.,
 397 as long as the discretization is sufficient to model the full wave
 398 behavior in the structure, the dispersion relation is guaranteed to
 399 be calculated. In addition, the matrices used for the numerical
 400 model are very small compared to those required by other
 401 methods, such as FEM, and are, therefore, much less demanding in
 402 terms of calculation.

403 Wavenumbers are perfectly symmetric with both
 404 $\text{Re}(k_1 h/2\pi) = 0$ and $\text{Im}(k_1 h/2\pi) = 0$ axis, which is a feature of
 405 reciprocal systems. Wavenumbers having a very large slope and a
 406 low imaginary part correspond to modes mostly propagating in the
 407 aluminum plate. They are very close to the bulk longitudinal k_l and
 408 transverse k_t wavenumbers in the aluminum. This is due to the
 409 very large contrast between the elastic properties of the aluminum
 410 and those of the poroelastic frame. The other branches asymptotically
 411 tend toward the bulk acoustic, k_a , compression, k_p , or shear,
 412 k_s , wavenumbers of the poroelastic medium at high frequency. At
 413 low frequencies, these modes are highly dispersive.

414 If we compare these results with the dispersion relation
 415 depicted in Fig. 5(c) of Appendix B for the guided waves in a single
 416 poroelastic plate twice as thick and in the absence of the elastic
 417 plate, we find some essential differences. The branches associated with
 418 the elastic plate and the branch clearly associated with the
 419 coupling between the elastic and poroelastic layers [referenced as
 420 (1) in Fig. 5(c) of Appendix B] do not exist. The other branches are
 421 similar to those of this single poroelastic layer, although slightly
 422 modified by the presence of the elastic plate. This proves a weak

423 coupling between the elastic and poroelastic layers, particularly at
 424 high frequencies. At lower frequencies, the coupling between the
 425 two layers is stronger. Effectively, the wavelength is much larger
 426 than the thickness of at least one of the two layers in these fre-
 427 quency ranges, which favors coupling. The A_0 branch observed in
 428 the case of a single poroelastic layer disappears in the two-layer
 429 system rigidly backed, because this rigid backing does not allow the
 430 existence of such a mode.

431 C. Mode shapes and energy fluxes

432 Beyond the SCM numerical efficiency, a significant advantage
 433 of the method is that the eigenvectors associated with each eigen-
 434 value directly provide the associated mode shape. Since these mode
 435 shapes, i.e., eigenvectors, are calculated from an eigenvalue
 436 problem, their amplitudes are defined up to a constant. They are
 437 normalized to the value of the pressure field at the bottom of the
 438 poroelastic layer, i.e., at the location of the rigid backing, because
 439 this condition imposes $\tilde{u}^{(1)}(0) = 0$ (and, in particular, $\tilde{u}_2^{(1)}(0) = 0$),
 440 which is equivalent to a maximum pressure field. From these nor-
 441 malized eigenvectors, any physical fields can be calculated as
 442 detailed in Appendix C.

443 Let us consider two solutions $k_1^\pm = \pm |\text{Re}(k_1)|$ symmetric in
 444 the dispersion diagram with respect to the axis $\text{Re}(k_1) = 0$ as shown
 445 in Figs. 3(a) and 3(b). The displacement fields and total energy
 446 fluxes in each direction are depicted in Figs. 3(c)–3(f). The results
 447 calculated using the SCM method, plotted in continuous lines,
 448 match those obtained using the Müller method, plotted with marker
 449 lines. These two modes are identical but propagate in opposite direc-
 450 tions; i.e., the mode k_1^+ propagates toward positive x_1 , while the
 451 mode k_1^- propagates toward negative x_1 . Displacement fields and
 452 energy fluxes are identical along the x_2 axis but are of equal modulus
 453 but opposite signs along the x_1 axis [see Figs. 3(c)–3(f)]. Both dis-
 454 placement field and energy flux amplitudes are two to three orders
 455 of magnitude smaller in the elastic plate (for $h_1 < x_2 < h$) than in
 456 the poroelastic plate. The aluminum coating is almost acting as a
 457 rigid boundary condition, as also testified by the fact that the x_1
 458 components of the displacement field and energy fluxes are almost
 459 symmetric with respect to the axis $x_2 = h_1/2$, while their x_2 compo-
 460 nents are almost antisymmetric along the x_2 axis. Note that the fluid
 461 phase Poynting vectors depicted in Fig. 3(f) are of equal modulus
 462 but opposite signs, symmetric with respect to the axis $x_2 = h_1/2$,
 463 and more than 100 times smaller than the total energy flux in ampli-
 464 tude. The energy of these modes is, thus, mainly localized in the
 465 solid phase of the poroelastic plate.

466 To go a step further, we evaluated the energy transport veloc-
 467 ity $\bar{V}_e = \bar{P}_t/\bar{U}$ as the ratio between the average energy flux in each
 468 layer \bar{P}_t over the mean total energy \bar{U} . The energy transport veloc-
 469 ity of the mode highlighted in orange in Figs. 3(a) and 3(b) is com-
 470 pared to the group velocity $v_g = \partial\omega/\partial\text{Re}(k_1)$ ⁴⁶ in Fig. 3(g). It is
 471 numerically computed by doing finite differences on a branch of
 472 the dispersion relation. Both velocities match for frequency ranges
 473 where the imaginary part of k_1 is low, i.e., for weak attenuation
 474 modes,^{47–50} but are different for strong attenuation. In particular,
 475 the group velocity diverges around the cut-on frequency. This is
 476 the reason why the energy transport velocity is usually preferred to
 477 study absorbing structures. The energy transport velocity \bar{V}_e of the

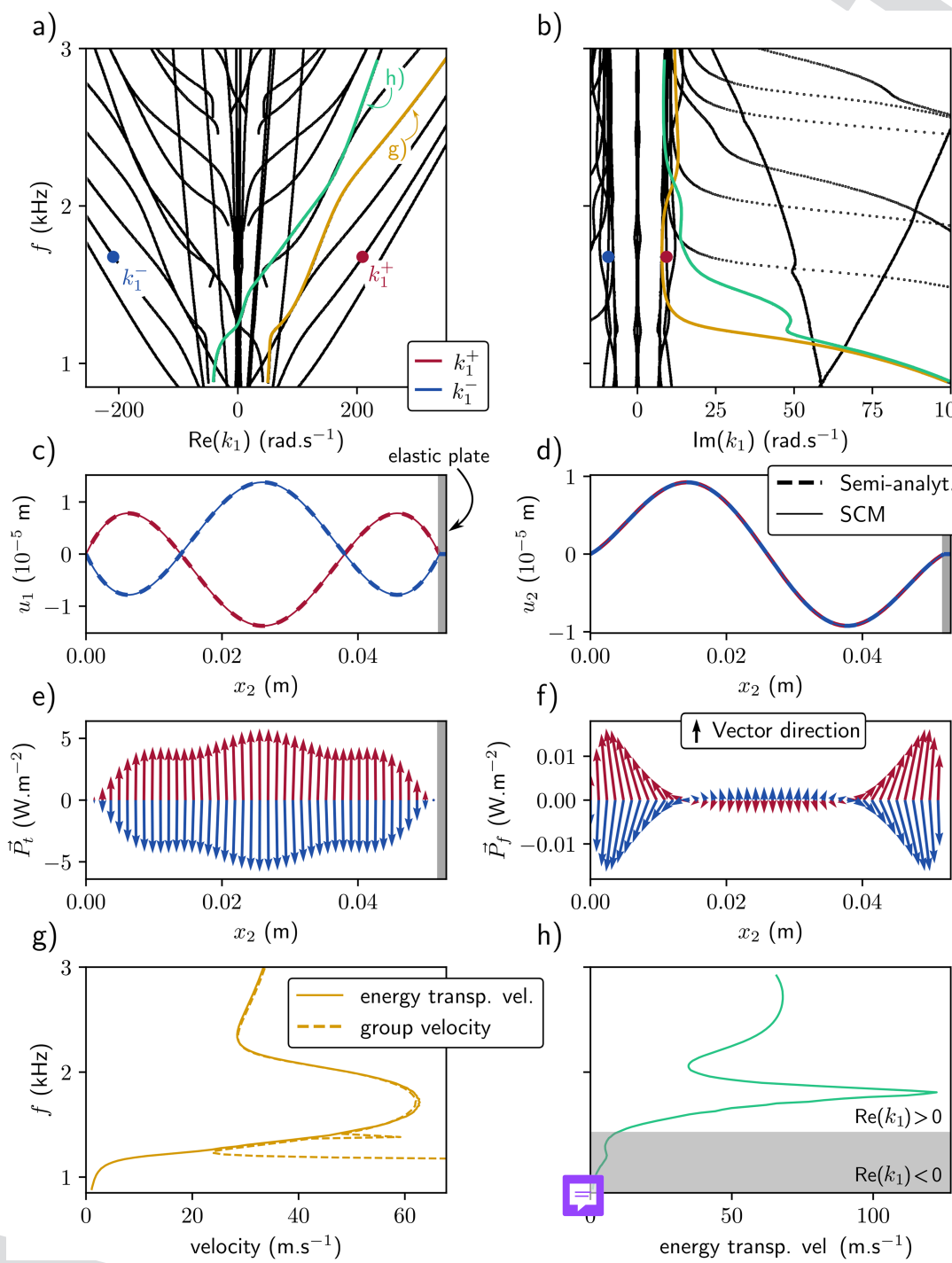


FIG. 3. (a) and (b) represent the real and imaginary parts of the dispersion relation of the two-layer structure. Two branches are highlighted in yellow and green, as well as two specific solutions, k_1^- (blue) and k_1^+ (red), symmetric with respect to the $\text{Re}(k_1) = 0$ axis. Displacement fields in the x_1 (c) and x_2 direction (d) associated with the k_1^+ and k_1^- solutions are displayed. The total Poynting (e) vector and the fluid Poynting vector (f) with the length of the arrow indicating the amplitude and angle indicating the direction of the vector field. (g) Group and energy transport velocities for the yellow branch. (h) Energy transport velocity for the green branch. The gray area represents the frequency range over which this velocity is negative.

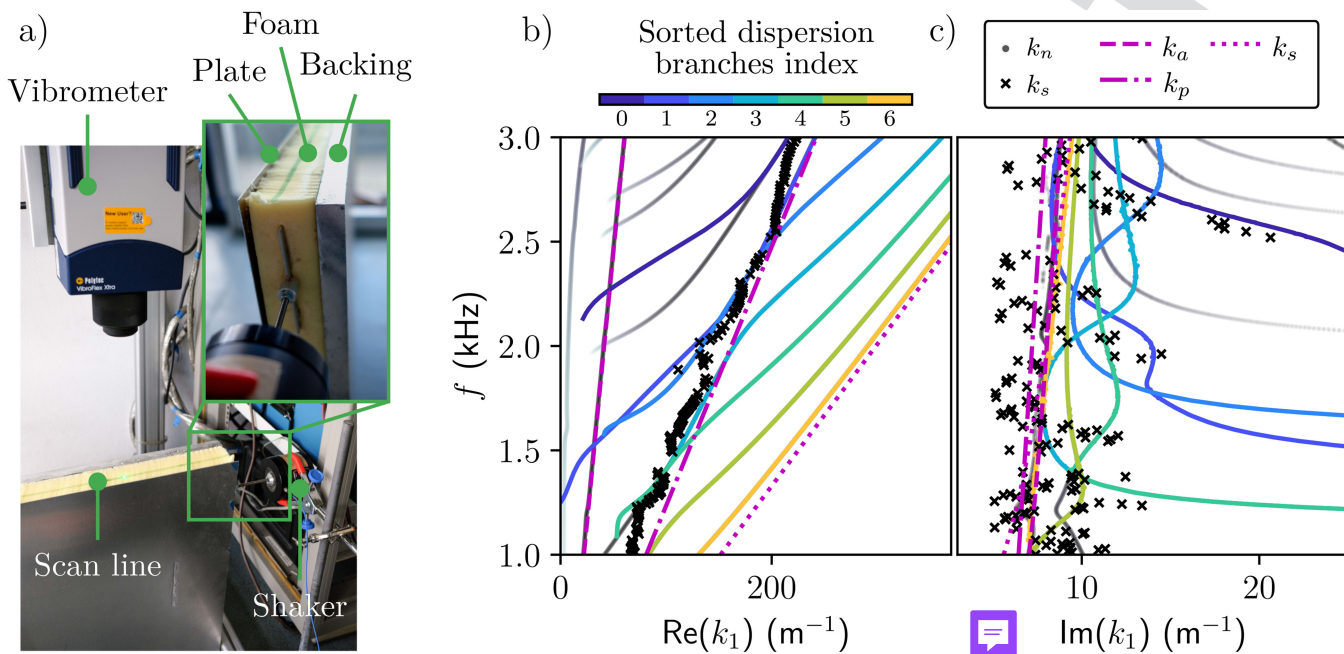


FIG. 4. (a) Experimental setup used for the measurement of the normal displacement field of the two-layer structure, with a close-up of the sample excitation. (b) Real and (c) imaginary parts of the dispersion relations recovered experimentally from the SLaTCoW method k_s (black crosses) and calculated from the SCM k_s (colored lines and black-to-gray dots) and the bulk wavenumbers in the poroelastic material (magenta lines).

478 mode highlighted in green in Figs. 3(a) and 3(b) is depicted in 479 Fig. 3(h). This energy transport velocity is always positive, while k_1 480 crosses the $\text{Re}(k_1) = 0$ axis. When $\text{Re}(k_1) < 0$, the phase velocity is 481 negative, while $\text{Im}(k_1) > 0$. This branch (and the symmetric one) 482 has also a negative group velocity as also testified by the fact 483 $\text{Re}(k_1) < 0$ while $\text{Im}(k_1) > 0$ in the shaded area in Fig. 3(h). This 484 branch has also an exponentially growing amplitude.

485 D. Experimental validation

486 The experimental set-up is depicted in Fig. 4(a). The sample is 487 the two-layer structure considered in Subsection III C. The aluminum 488 plate is glued on top of the poroelastic layer. The latter layer 489 is glued on a 3 cm-thick aluminum plate, which mimics the rigid 490 backing. The three elements are 45 cm wide and 85 cm long. The 491 surrounding medium and the saturating fluid are air, at regular 492 pressure and temperature conditions. The sample is positioned 493 perpendicularly to the ground on its longest side as depicted in 494 Fig. 4(a) to ease the mode excitation in the poroelastic layer. The 495 excitation is provided by a shaker (Brüel and Kjaer type 4810), 496 which is rigidly attached to the sample with a threaded steel rod 497 fixed to the shaker on one side and glued on a 1 mm thick aluminum 498 plate of width 10 cm and height 1.5 cm. This plate is cut at 499 the edge opposite to the threaded steel rod and glued to the porous 500 sample, creating a line source at the edge of the sample. The resonance 501 of this part was measured to be 4500 Hz, which is the upper 502 limit of the measured frequency range. The excitation signal is a

swept-sine function with 400 points ranging from 1 kHz to 3 kHz. 503 The general layout of the experiments is similar to that used originally 504 in Ref. 51. The key difference in our case is that the excitation 505 is operated directly to the poroelastic layer and not to the top of 506 the aluminum plate, because the modes that correspond to propagating 507 solutions in the poroelastic layer are encapsulated in 508 between two almost rigid plates (see Sec. III C). The normal dis- 509 placement is measured with a laser Doppler vibrometer (Polytec 510 VibroFlex Neo) on a line of length $L = 40$ cm, along the side of the 511 thickness of the porous layer. These measurements are averaged 512 100 times. The excitation signal and the measured field are inter- 513 faced through a computer via a Zürich Instruments acquisition 514 card.

The SLaTCoW method is used to analyze the space-frequency 516 displacement measurements and recover the complex wavenumber- 517 real frequency dispersion relation. This method relies on the Laplace 518 spatial transform of these measurements, which gives access to the 519 real and imaginary components of the complex wavenumber. The 520 difference between this Laplace transform and a correctly chosen 521 ansatz function is finally minimized for each frequency, to recover 522 the dispersion relation. More details on this method are given in 523 Appendix E as well as in the original article.⁵¹ The complex wave- 524 number-real frequency dispersion relation in Figs. 4(b) and 4(c) 525 depicts the wavenumbers recovered experimentally k_s and simulated 526 k_n . Four modes were sought during the minimization with the 527 SLaTCoW method: three of them correspond to the three bulk waves 528 due to excitation and the fourth is depicted. The experimentally 529

530 recovered mode jumps from one branch to the other because of the
 531 large modal density. The cut-on frequencies of the modes are clearly
 532 visible, especially on the imaginary part of the wavenumber. The
 533 lower real wavenumber parts of the numerical dispersion relation are
 534 not retrieved with the experimental results. This is because they cor-
 535 respond to high attenuation of the mode, a part that is inherently
 536 difficult to measure in this experimental conditions. Generally, the
 537 recovered branches are those around the bulk solid compression
 538 wavenumber, corresponding to the wave that we most probably
 539 excite in the structure. The difficulties in efficiently exciting all the
 540 guided waves supported by this configuration largely explain the
 541 missing curves in the dispersion relation. The location and orienta-
 542 tion of the excitation line limit possible symmetries and the genera-
 543 tion of potential shear waves. This choice was made to avoid the
 544 main excitation of guided waves in the elastic plate when excitation
 545 and displacement measurement are performed only on this element.
 546 In addition, the modes mainly supported by the fluid phase should
 547 also be better excited by a loudspeaker and, therefore, better mea-
 548 sured by a microphone. However, we have chosen to focus on the
 549 modes mainly supported by the solid phase. Nevertheless, the agree-
 550 ment between experimental results and simulation is quite good,
 551 thus validating the method.

552 IV. CONCLUSION

553 A spectral collocation method (SCM) is proposed to calculate
 554 dispersion relations for guided acoustic wave propagation in multi-
 555 layer structures. The formalism is general enough to be able to con-
 556 sider arbitrary arrangements of (visco-) elastic, poroelastic, and
 557 (viscothermal-) fluid layers. Outgoing fluid radiation, leading to leaky
 558 modes, can be accounted for. The fields in each layer
 559 are approximated by Chebyshev polynomials and discretized on the
 560 corresponding nodes. Interface conditions are implemented to couple
 561 layers together. The solution provides the full complex wavenumber-
 562 real frequency dispersion relation of the considered structure. In addition,
 563 the physical fields in each layer are directly evaluated since they
 564 are the eigenvectors associated with the eigenvalue problem giving
 565 the dispersion relation. The dispersion diagram calculated with the
 566 present SCM is validated against experimental results and that calcu-
 567 lated with a root-finding method (Müller method) in a simple two-
 568 layer structure consisting of a rigidly backed poroelastic layer covered
 569 by a thin aluminum plate radiating in a fluid half-space. The semi-
 570 analytical approach underlying the root-finding method is taken a
 606

step further to solve for the wave amplitudes as well, providing a ref-
 571 erence for the mode shapes calculated with the SCM. The dispersion
 572 properties in such structures, as well as the direction of the energy
 573 density in each phase of the poroelastic layers using a decoupled
 574 expression for the Poynting vectors, are analyzed. Results on the
 575 energy transport velocity are also reported.
 576

This method paves the way for complex wavenumber-real fre-
 577 quency dispersion relation calculations and analysis of more
 578 complex structures, such as layers with embedded periodic inclu-
 579 sions (elastic or resonant), i.e., metaporoelastic surfaces.
 580

AUTHOR DECLARATIONS

Conflict of Interest

The authors have no conflicts to disclose.

Author Contributions

Mathieu Maréchal: Formal analysis (equal); Investigation (equal);
 585 Methodology (equal); Software (equal); Visualization (lead);
 586 Writing – original draft (lead); Writing – review & editing (equal).
 587

Alan Geslain: Data curation (equal); Investigation (equal);
 588 Validation (equal); Writing – review & editing (supporting).
 589

Jean-Philippe Groby: Formal analysis (supporting); Methodology
 590 (equal); Supervision (lead); Writing – review & editing (lead).
 591

Vicente Romero-García: Formal analysis (supporting);
 592 Methodology (supporting); Supervision (supporting); Writing –
 593 review & editing (supporting). **Olivier Dazel:** Formal analysis
 594 (equal); Investigation (equal); Methodology (equal); Supervision
 595 (equal); Writing – review & editing (equal).
 596

DATA AVAILABILITY

The data that support the findings of this study are available
 598 from the corresponding author upon reasonable request.
 599

APPENDIX A: EXPRESSION OF THE BIOT ELASTIC COEFFICIENTS AND EFFECTIVE PARAMETERS IN POROELASTIC MATERIALS

The complex and frequency dependent density and bulk
 603 modulus of the fluid phase, which accounts, respectively, for the
 604 viscous and thermal losses are^{23,24} as
 605

$$\rho_{\text{eq}}(\omega) = \frac{\rho_f \alpha_\infty}{\phi} \left(1 + \frac{iR_f \phi}{\rho_f \alpha_\infty \omega} \sqrt{1 - i\omega \rho_f \mu_f \left(\frac{2\alpha_\infty}{R_f \phi \Lambda} \right)^2} \right), \quad (\text{A1})$$

$$K_{\text{eq}} = \frac{\kappa P_0}{\phi} \left(\kappa - (\kappa - 1) \right) \left/ \left(1 + iR_f \phi \rho_f \alpha_\infty \text{Pr} \omega \sqrt{1 - i\text{Pr} \omega \rho_f \mu_f \left(\frac{2\alpha_\infty}{R_f \phi \Lambda'} \right)^2} \right) \right)^{-1},$$

608 resistivity, μ_f is the dynamic viscosity, κ is the heat capacity ratio, ρ_f 612
 609 is the density of the saturating fluid, and P_0 is the ambient pressure. 613

610 where ϕ is the porosity, α_∞ is the tortuosity, Λ and Λ' are, respec-
 611 tively, the viscous and thermal characteristic lengths, R_f is the flow

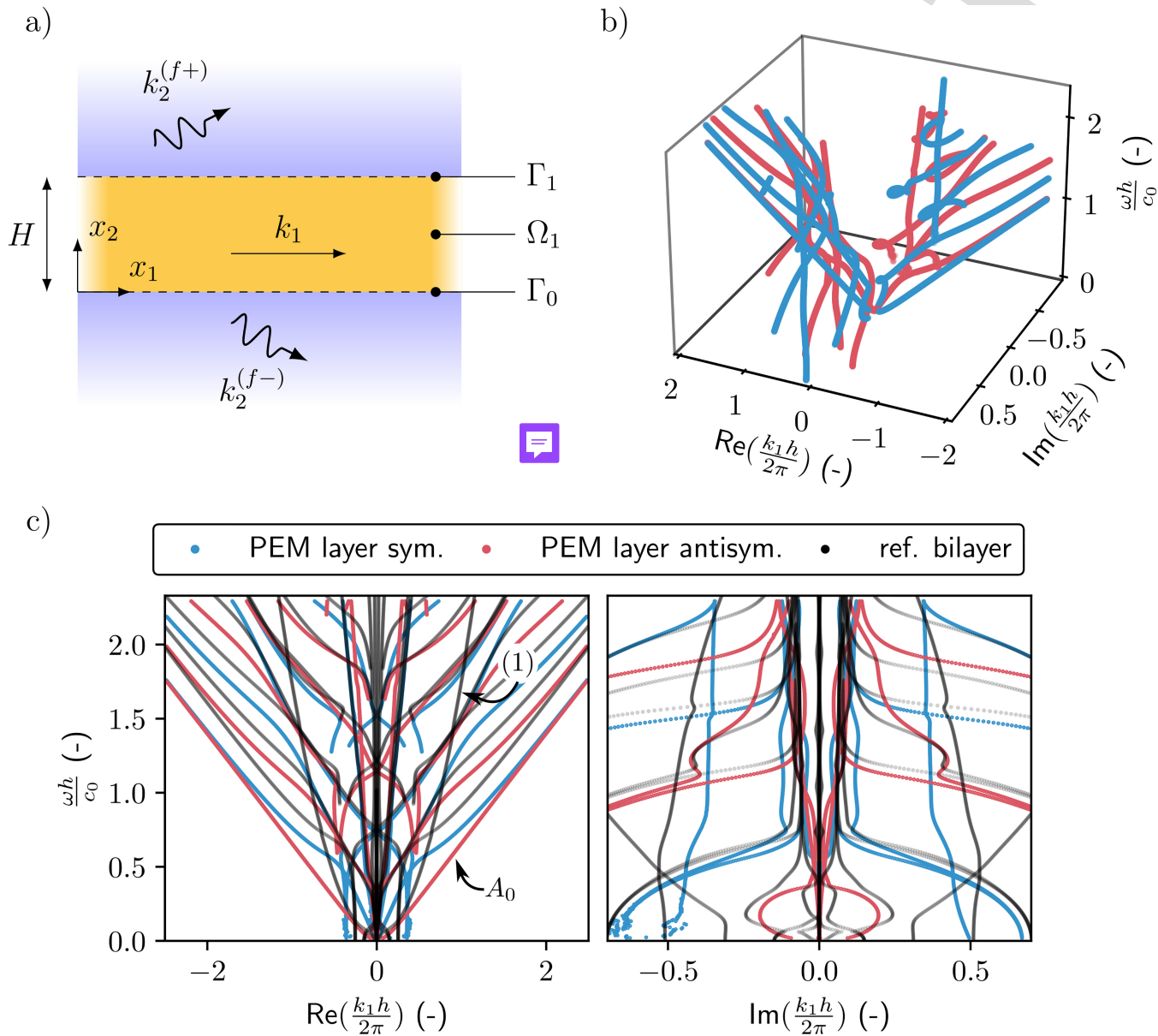


FIG. 5. (a) Sketch of the single layer poroelastic structure geometry. (b) 3D view of the complex wavenumber-real frequency dispersion relation and (c) real and imaginary parts of the dispersion relation. The branches of the symmetric and antisymmetric modes are represented by blue and red curves, respectively. The dispersion relation of the two-layer elastic-poroelastic system studied in Sec. III is reminded with black lines.

614 The Biot elastic coefficients, P , Q , and R , are more commonly
 615 expressed in terms of the frame, K_b , effective fluid, K_{eq} , and shear,
 616 N_s , moduli when saturated by a light fluid as

$$P = K_b + \frac{4}{3}N_s + (1 - \phi)^2 \frac{K_{eq}}{\phi}, \quad Q = K_f(1 - \phi), \quad R = \phi K_{eq}, \quad (\text{A2})$$

while the apparent densities are

$$\rho_{22} = \phi^2 \rho_{eq}, \quad \rho_{12} = \phi \rho_f - \rho_{22}, \quad \rho_{11} = (1 - \phi)\rho_s - \rho_{12}, \quad (\text{A3})$$

with ρ_s being the density of the solid phase. The coefficients in Eq. (13) are, thus,

$$\begin{aligned} \hat{A} &= K_b - \frac{2}{3} N_s + \frac{K_{eq}}{\phi} ((1 + (1 - \phi)), \\ \hat{\rho} &= \rho_1 + \phi \rho_f - 2\phi^2 \rho_{eq} - \frac{\rho_f^2}{\rho_{eq}} \\ \beta &= \frac{\rho_f}{\rho_{eq}} - 2\phi - 1, \end{aligned} \quad (\text{A4})$$

where $\rho_1 = \phi \rho_f + (1 - \phi) \rho_s$ is the apparent density of the frame. Finally, the frame bulk modulus and the shear modulus are linked by the Poisson ratio ν with $K_b = 2N_s(1 + \nu)/3(1 - 2\nu)$.

638

$$\left(1 + \phi + \phi \frac{\rho_{12}}{\rho_{22}}\right) u_2^{(1)} + \frac{\phi^2}{\rho_{22}\omega^2} \partial_2 p^{(1)} = u_2^{(0\pm)}, \quad p^{(1)} = p^{(0\pm)}, \quad \hat{\sigma}_{22}^s = \left(1 - \phi \left(1 + \frac{Q}{R}\right)\right) p^{(0\pm)}, \quad \hat{\sigma}_{12}^s = 0. \quad (\text{B1})$$

The discretized form of these boundary conditions is

$$\underline{\underline{C}}_1 = \begin{pmatrix} \phi^2 \rho_{22} D_2^+ & 0 & \omega^2 \left(1 + \phi \left(1 + \frac{\rho_{12}}{\rho_{22}}\right)\right) I^+ & ik_2^{(f)} \rho_f \\ 0 & 0 & 0 & -ik_2^{(f)} \rho_f \\ 0 & ik_1 (\hat{P} - 2N_s) I^+ & \hat{P} D_2^+ & 1 - \phi \left(1 + \frac{Q}{R}\right) \\ 0 & N_s D_2^+ & ik_1 N_s I^+ & 0 \end{pmatrix}. \quad (\text{B2})$$

643

644

These matrices are then arranged in the same manner as Eq. (10), and the wavenumbers are calculated. Figures 5(b) and 5(c) depict the results.

In a similar way as Lamb modes, the different modes can be sorted in symmetric and antisymmetric modes. This is done by comparing the sign of the radiated amplitudes at each edge of the layer. Results are shown in Fig. 5(b). All modes necessarily have an imaginary part, both because of the radiation condition, i.e., leakage, and because of viscothermal dissipation as can be noticed in Fig. 5(c).

APPENDIX C: EVALUATION OF THE PHYSICAL FIELDS FROM THE SCM SOLUTIONS

The discrete sets of eigenvectors resulting from the SCM are the spatial Laplace transforms of some physical fields at collocation points, i.e., the locations where the discrete equations of motion (residue) are exactly satisfied. These discrete fields are interpolated into a continuous form using

$$\mathbf{s}^{(n)}(x_2) = \left[\underline{\underline{\psi}}_m^{-1}(\xi) \underline{\underline{\xi}}_m^{(n)}(\xi) \right] \boldsymbol{\psi}(\xi^{(n)}), \quad (\text{C1})$$

where the terms in brackets correspond to the coefficients $\alpha_m^{(n)}$ given in Eq. (8). The Chebyshev polynomials $\boldsymbol{\psi}$ are the basis that maps from the discrete grid ξ back to the physical space.

APPENDIX B: APPLICATION TO A SINGLE POROELASTIC LAYER SURROUNDED BY TWO FLUID HALF-SPACES

625
626
627

The dispersion relation of guided waves in a single layer of poroelastic material surrounded by two identical fluid half-spaces is considered [see Fig. 5(a)]. The poroelastic material properties are those considered in Sec. III B and the layer thickness is $2h^{(1)} = 104$ mm, i.e., twice the thickness of the poroelastic layer considered in the two-layer system.

The discretized equations of motion are that provided in Eq. (16). $M^{(1)} = 11$ collocation points are considered. Only the boundary conditions at the lower, i.e., Γ_0 at $x_2 = 0$, and upper, i.e., Γ_1 at $x_2 = h$, interfaces are modified. They read as⁴⁵

The stress tensor components depend on the direct expressions of the fields and their first-order derivative in x_2 , denoted with a prime symbol in the following. The various fields, differentiated up to any order, can be calculated by replacing $\boldsymbol{\psi}$ by its derivative in Eq. (C1). Explicit expressions are given in the following,

- in the elastic layer, the spatial Laplace transforms of stress tensor components are computed from $\tilde{\mathbf{u}}$, with

$$\begin{aligned} \tilde{\sigma}_{11} &= (\lambda + 2\mu) ik_1 \tilde{\mathbf{u}}_1 + \lambda \tilde{\mathbf{u}}'_2, & \tilde{\sigma}_{12} &= \mu (\tilde{\mathbf{u}}'_1 + ik_1 \tilde{\mathbf{u}}_2), \\ \tilde{\sigma}_{22} &= \lambda ik_1 \tilde{\mathbf{u}}_1 + (\lambda + 2\mu) \tilde{\mathbf{u}}'_2. \end{aligned} \quad (\text{C2})$$

- in the poroelastic layer, the full solid stress tensor is expressed as $\tilde{\boldsymbol{\sigma}}_s = \hat{\boldsymbol{\sigma}}_s - \phi(Q/R)\tilde{\mathbf{p}}$, with $\hat{\boldsymbol{\sigma}}_s$ being the spatial Laplace transform of the *in vacuo* solid stress tensor introduced in Sec. III. The components of this full solid stress tensor are

$$\begin{aligned} \tilde{\sigma}_{s,11} &= P ik_1 \tilde{\mathbf{u}}_{s,1} + \hat{A} \tilde{\mathbf{u}}'_{s,2} - \phi \frac{Q}{R} \tilde{\mathbf{p}}, & \tilde{\sigma}_{s,12} &= N_s \left(\tilde{\mathbf{u}}'_{s,1} + ik_1 \tilde{\mathbf{u}}_{s,2} \right), \\ \tilde{\sigma}_{s,22} &= \hat{A} ik_1 \tilde{\mathbf{u}}_{s,2} + P \tilde{\mathbf{u}}'_{s,1} - \phi \frac{Q}{R} \tilde{\mathbf{p}}. \end{aligned} \quad (\text{C3})$$

The Laplace transform of the fluid stress tensor is calculated as

$$\tilde{\boldsymbol{\sigma}}_f = -\phi \tilde{\mathbf{p}} \delta_{ij}, \quad (\text{C4})$$

678 and the fluid displacement components are

$$\tilde{u}_{f,1} = \frac{\phi}{\rho_{22}\omega^2} ik_1 \tilde{p} - \frac{\rho_{12}}{\rho_{22}} \tilde{u}_{s,1}, \quad \tilde{u}_{f,2} = \frac{\phi}{\rho_{22}\omega^2} \tilde{p}' - \frac{\rho_{12}}{\rho_{22}} \tilde{u}_{s,2}. \quad (\text{C5})$$

679

680 All physical fields $\theta(\mathbf{x})$ can finally be calculated by the inverse
681 spatial Laplace transform with $\theta(\mathbf{x}) = \tilde{\theta}(k_1, x_2) e^{ik_1 x_1}$.

689

$$\begin{aligned} & - \int_{\partial\Omega} (-\boldsymbol{\sigma}_s \cdot \mathbf{v}_s^*) \cdot \mathbf{n} + (-\boldsymbol{\sigma}_f \cdot \mathbf{v}_f^*) \cdot \mathbf{n} dS = \\ & \quad \frac{1}{2} \int_{\Omega} \rho_1 \partial_t |\mathbf{v}_s|^2 - \rho'_{12} \partial_t (\mathbf{v}_f - \mathbf{v}_s)^2 + \rho_2 \partial_t |\mathbf{v}_f|^2 d\Omega \\ & \quad + \int_{\Omega} \boldsymbol{\sigma}_s : \partial_t \boldsymbol{\epsilon}_s^* + \boldsymbol{\sigma}_f : \partial_t \boldsymbol{\epsilon}_f^* - b(\mathbf{v}_s - \mathbf{v}_f)^2 d\Omega, \end{aligned} \quad (\text{D1})$$

690

692

693 where $\mathbf{v}_s = \partial_t \mathbf{u}_s$ and $\mathbf{v}_f = \partial_t \mathbf{u}_f$ are the velocity fields, $\boldsymbol{\sigma}_s$ and $\boldsymbol{\sigma}_f$
694 are the stress tensors, $\boldsymbol{\epsilon}_s = 1/2(\nabla \mathbf{u}_s + \nabla^T \mathbf{u}_s)$ and
695 $\boldsymbol{\epsilon}_f = 1/2(\nabla \mathbf{u}_f + \nabla^T \mathbf{u}_f)$ are the strain tensors in the solid frame
696 and in the fluid phase, respectively, and $*$ denotes the complex con-
697 jugate. Note that a similar expression is provided in Ref. 50 where
698 the alternative 1962 Biot formulation is used.

699

700 The left-hand side contains the energy density flux
701 $P_s = -\boldsymbol{\sigma}_s \cdot \mathbf{v}_s^*$ and $P_f = -\boldsymbol{\sigma}_f \cdot \mathbf{v}_f^*$ in the elastic frame and the fluid
702 phase. The right-hand side contains the kinetic energy K^{43} and the
703 internal forces $P_{\text{int}} = \partial_t W + P_{\text{dis}}$. The latter is the sum of the time
704 derivative of the strain energy W and the dissipated power P_{dis} by
705 the elastic damping and the viscous and thermal losses.⁵² In the
706 frequency domain, the kinetic and strain energies read as

$$\begin{aligned} K &= \frac{1}{2} \rho_1 \partial_t |\mathbf{v}_s|^2 - \frac{1}{2} \rho'_{12} \partial_t (\mathbf{v}_f - \mathbf{v}_s)^2 + \frac{1}{2} \rho_2 \partial_t |\mathbf{v}_f|^2, \\ W &= \frac{1}{2} \hat{\boldsymbol{\sigma}}_s : \boldsymbol{\epsilon}_s^* + \frac{1}{2} R \nabla \cdot (Q \mathbf{u}_s + R \mathbf{u}_f). \end{aligned} \quad (\text{D2})$$

707 Finally, the time average total Poynting vector is $\langle \mathbf{P}_t \rangle = \langle \mathbf{P}_s \rangle + \langle \mathbf{P}_f \rangle$,
708 with $\langle \mathbf{P}_s \rangle = -\text{Re}(\boldsymbol{\sigma}_s \cdot \mathbf{v}_s^*)/2$ and $\langle \mathbf{P}_f \rangle = -\text{Re}(\boldsymbol{\sigma}_f \cdot \mathbf{v}_f^*)/2$, and the
709 total energy density is $\langle U \rangle = \langle K \rangle + \langle W \rangle = \text{Re}(K)/2 + \text{Re}(W)/2$.
710 Note that a similar procedure can be followed for an isotropic elastic
711 or fluid medium.⁵³ In particular, the elastic Poynting vector is
712 $\langle \mathbf{P} \rangle = \text{Re}(\boldsymbol{\sigma} \cdot \mathbf{v}^*)/2$, where $\boldsymbol{\sigma}$ is the stress tensor and \mathbf{v} is the velocity
713 in the elastic medium.

714 The energy transport velocity V_e is evaluated from the latter
715 expressions,

$$V_e = \frac{\langle \mathbf{P}_t \rangle \cdot \mathbf{n}}{\langle U \rangle}. \quad (\text{D3})$$

716 When a multi-layer configuration is considered, the latter velocity
717 is averaged over the structure thickness $\bar{V}_e = \bar{P} \bar{U}$, with the average
718 Poynting vector and the average total energy defined as

APPENDIX D: ENERGY FLUX IN THE MULTILAYER STRUCTURE—POYNTING THEOREM IN A POROELASTIC MEDIUM

Energy conservation is commonly conducted in the time
domain. Let us consider a volume Ω , bounded by $\partial\Omega$, with \mathbf{n} being
the outgoing normal vector. The energy balance or Poynting
theorem in a poroelastic material reads as^{19,52}

$$\bar{P}_t = \sum_n \frac{1}{h_n} \int_{h_{n-1}}^{h_n} \langle \mathbf{P}_t^{(n)} \rangle \cdot \mathbf{e}_{x_2} dx_2, \quad \bar{U} = \sum_n \frac{1}{h_n} \int_{h_{n-1}}^{h_n} \langle U^{(n)} \rangle dx_2. \quad (\text{D4})$$

APPENDIX E: REMINDER OF THE SLATCOW METHOD FOR OBTAINING COMPLEX-VALUED WAVENUMBERS

The key point of the SLaTCoW method is the Laplace trans-
form, $\mathfrak{L}_{\text{mes}}(z)$ with $z = z_r + iz_i$ being the Laplace space coordinate,
of the data measured in space at a fixed frequency ω . In doing so,
we move from the spatial domain to the complex wavenumber
domain. The difference between $\mathfrak{L}_{\text{mes}}(z)$ and the spatial Laplace
transform of the displacement ansatz along the same line, $\mathfrak{L}_{\text{rec}}(z)$,
is then minimized in the least square sense to recover both the
complex amplitude (magnitude and phase) and the complex wave-
number of each mode assumed to be part of the displacement
ansatz.

The experimental Laplace spatial transform $\mathfrak{L}_{\text{mes}}(z) = \int_0^L r(x) e^{-izx} dx$ is computed at each frequency ω from the transfer
function $r(x)$ between the excitation and the normal displacement
measured along a line $x \in [0, L]$, with $L = 0.3$ m and spacing
 $d_x = 0.001$ m. The displacement ansatz is assumed to be of the
form $w(x) = \sum_{\beta} A^{\beta} e^{ik^{\beta} x}$, with β being the number of guided waves,
i.e., the number of modes, and where $A^{\beta} = |A^{\beta}| e^{i\phi^{\beta}}$ is the complex
amplitude and k^{β} is the complex wavenumber of the β th mode. In
practice, β is the smallest integer that gives a good fit between the
two Laplace transforms and, therefore, depends on the frequency
under consideration. Its spatial Laplace transform reads as

$$\mathfrak{L}_{\text{rec}}(z) = \sum_{\beta} A^{\beta} L e^{i(k^{\beta} - z)\frac{L}{2}} \text{sinc}\left((k^{\beta} - z)\frac{L}{2}\right).$$

The cost function $\mathfrak{C} = (\mathfrak{L}_{\text{rec}}(z) - \mathfrak{L}_{\text{mes}}(z))/\mathfrak{L}_{\text{mes}}(z)$ is finally
minimized using the MATLAB function `fminsearchbnd` for
 $\{|A^{\beta}|, \phi^{\beta}, \text{Re}(k^{\beta}), \text{Im}(k^{\beta})\}, \forall \beta$. The initial guess is the recovered
values of the minimization parameters at the previous frequency,
with the exception of the first frequency. The method is graphically
exposed in Fig. 6. Figures 6(c) and 6(d) depict the complex disper-
sion relation as already depicted in Fig. 4. Figure 6(a) depicts the

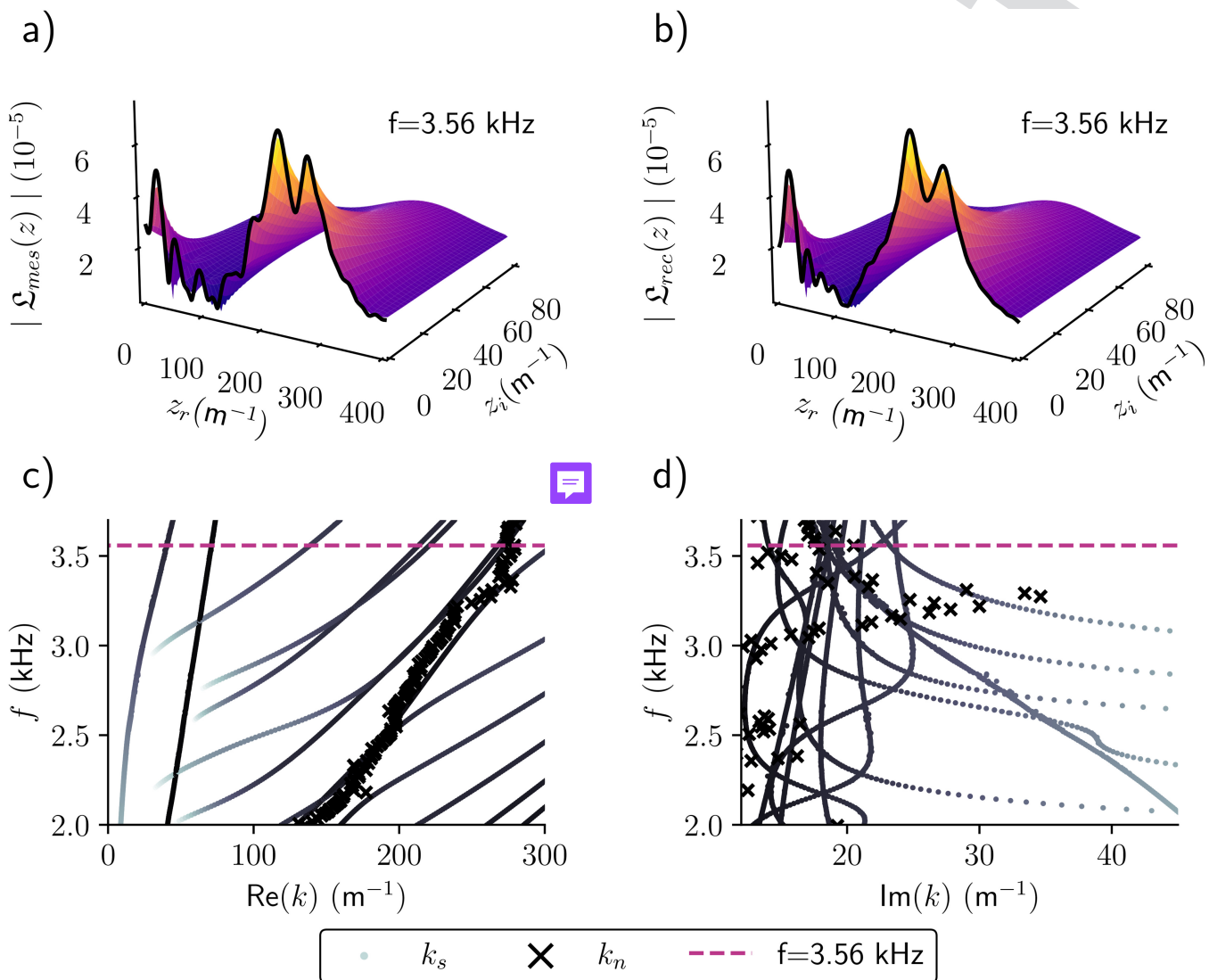


FIG. 6. Description of the procedure of the SLaTCoW method: (a) Spatial Laplace transform from the experimental data. (b) Spatial Laplace transform of the reconstructed wave fields. Real (c) and imaginary (d) parts of the experimentally retrieved wavenumbers (crosses) compared to the SCM (black-to-gray dots). The frequency at which the Laplace transforms are represented corresponds to the magenta dashed line in the graph.

751 spatial Laplace transform of the experimental data, and Fig. 6(b)
 752 depicts $\Omega_{rec}(z)$ with the parameters derived from minimization of
 753 the cost function at the frequency $f = 3.56$ kHz. This frequency is
 754 highlighted by the purple dashed line in Figs. 6(c) and 6(d). The
 755 two Laplace transforms match almost perfectly.

756 REFERENCES

757 ¹P. Kowalczyk and W. Marynowski, “Efficient complex root tracing algorithm
 758 for propagation and radiation problems,” *IEEE Trans. Antennas Propag.* **65**(5),
 759 2540–2546 (2017).

²P. S. Dubbelday, “Application of a new complex root-finding technique to the dispersion relations for elastic waves in a fluid-loaded plate,” *SIAM J. Appl. Math.* **43**(5), 1127–1139 (1983).

³D. E. Muller, “A method for solving algebraic equations using an automatic computer,” *Math. Tabl. Other Aids Comput.* **10**(56), 208 (1956).

⁴B. Pavlakovic, M. Lowe, D. Alleyne, and P. Cawley, *Disperse: A General Purpose Program for Creating Dispersion Curves* (Springer US, Boston, MA, 1997), pp. 185–192.

⁵A. M. A. Huber and M. G. R. Sause, “Classification of solutions for guided waves in anisotropic composites with large numbers of layers,” *J. Acoust. Soc. Am.* **144**(6), 3236–3251 (2018).

⁶A. M. A. Huber, “Classification of solutions for guided waves in fluid-loaded viscoelastic composites with large numbers of layers,” *J. Acoust. Soc. Am.* **154**(2), 1073–1094 (2023).

- ⁷⁷³ F. Treyyssède, K. Nguyen, A.-S. Bonnet-BenDhia, and C. Hazard, "Finite element computation of trapped and leaky elastic waves in open stratified waveguides," *Wave Motion* **51**(7), 1093–1107 (2014).
- ⁷⁷⁴ I. Bartoli, A. Marzani, F. Lanza Di Scalea, and E. Viola, "Modeling wave propagation in damped waveguides of arbitrary cross-section," *J. Sound Vib.* **295**(3-5), 685–707 (2006).
- ⁷⁷⁵ A. Marzani, E. Viola, I. Bartoli, F. Lanza Di Scalea, and P. Rizzo, "A semi-analytical finite element formulation for modeling stress wave propagation in axisymmetric damped waveguides," *J. Sound Vib.* **318**(3), 488–505 (2008).
- ⁷⁷⁶ J. L. Rose, *Ultrasonic Guided Waves in Solid Media*, 1st ed. (Cambridge University Press, 2014).
- ⁷⁷⁷ *Spectral Methods: Fundamentals in Single Domains*, Scientific Computation, edited by C. Canuto (Springer, Berlin, 2006), with 19 Tables.
- ⁷⁷⁸ L. N. Trefethen, *Spectral Methods in MATLAB* (Society for Industrial and Applied Mathematics, 2000).
- ⁷⁷⁹ M. Lowe, "Matrix techniques for modeling ultrasonic waves in multilayered media," *IEEE Trans. Ultrason., Ferroelect., Freq. Contr.* **42**(4), 525–542 (1995).
- ⁷⁸⁰ N. A. Haskell, "The dispersion of surface waves on multilayered media," *Bull. Seismol. Soc. Am.* **43**(1), 17–34 (1953).
- ⁷⁸¹ V. Pagneux and A. Maurel, "Determination of Lamb mode eigenvalues," *J. Acoust. Soc. Am.* **110**(3), 1307–1314 (2001).
- ⁷⁸² M. Gallezot, F. Treyyssède, and L. Laguerre, "Contribution of leaky modes in the modal analysis of unbounded problems with perfectly matched layers," *J. Acoust. Soc. Am.* **141**(1), EL16–EL21 (2017).
- ⁷⁸³ E. Georgiades, M. J. S. Lowe, and R. V. Craster, "Leaky wave characterisation using spectral methods," *J. Acoust. Soc. Am.* **152**(3), 1487–1497 (2022).
- ⁷⁸⁴ D. A. Kiefer, M. Ponschab, S. J. Rupitsch, and M. Mayle, "Calculating the full leaky Lamb wave spectrum with exact fluid interaction," *J. Acoust. Soc. Am.* **145**(6), 3341–3350 (2019).
- ⁷⁸⁵ M. A. Biot, "Theory of propagation of elastic waves in a fluid-saturated porous solid. I. Low-frequency range," *J. Acoust. Soc. Am.* **28**(2), 168–178 (1956).
- ⁷⁸⁶ M. A. Biot, "Theory of propagation of elastic waves in a fluid-saturated porous solid. II. Higher frequency range," *J. Acoust. Soc. Am.* **28**(2), 179–191 (1956).
- ⁷⁸⁷ M. A. Biot, "Mechanics of deformation and acoustic propagation in porous media," *J. Appl. Phys.* **33**(4), 1482–1498 (1962).
- ⁷⁸⁸ M. A. Biot, "Generalized theory of acoustic propagation in porous dissipative media," *J. Acoust. Soc. Am.* **34**(9A), 1254–1264 (1962).
- ⁷⁸⁹ D. L. Johnson, J. Koplik, and R. Dashen, "Theory of dynamic permeability and tortuosity in fluid-saturated porous media," *J. Fluid Mech.* **176**(-1), 379 (1987).
- ⁷⁹⁰ Y. Champoux and J.-F. Allard, "Dynamic tortuosity and bulk modulus in air-saturated porous media," *J. Appl. Phys.* **70**(4), 1975–1979 (1991).
- ⁷⁹¹ D. Lafarge, P. Lemarinier, J. F. Allard, and V. Tarnow, "Dynamic compressibility of air in porous structures at audible frequencies," *J. Acoust. Soc. Am.* **102**(4), 1995–2006 (1997).
- ⁷⁹² T. Weisser, J.-P. Groby, O. Dazel, F. Gaultier, E. Deckers, S. Futatsugi, and L. Monteiro, "Acoustic behavior of a rigidly backed poroelastic layer with periodic resonant inclusions by a multiple scattering approach," *J. Acoust. Soc. Am.* **139**(2), 617–629 (2016).
- ⁷⁹³ L. Boeckx, P. Leclaire, P. Khurana, C. Glorieux, W. Lauriks, and J. F. Allard, "Investigation of the phase velocities of guided acoustic waves in soft porous layers," *J. Acoust. Soc. Am.* **117**(2), 545–554 (2005).
- ⁷⁹⁴ G. Belloncle, H. Franklin, F. Luppé, and J. Conoir, "Normal modes of a poroelastic plate and their relation to the reflection and transmission coefficients," *Ultrasonics* **41**(3), 207–216 (2003).
- ⁷⁹⁵ J. F. Allard, M. Henry, and V. Garetton, "Pseudo-surface waves above thin porous layers (L)," *J. Acoust. Soc. Am.* **116**(3), 1345–1347 (2004).
- ⁷⁹⁶ J.-P. Groby, A. Wirgin, and E. Ogam, "Acoustic response of a periodic distribution of macroscopic inclusions within a rigid frame porous plate," *Waves Random Complex Media* **18**(3), 409–433 (2008).
- ⁷⁹⁷ F. Seyfaddini, H. Nguyen-Xuan, and V.-H. Nguyen, "Semi-analytical IGA-based computation of wave dispersion in fluid-coupled anisotropic poroelastic plates," *Int. J. Mech. Sci.* **212**, 106830 (2021).
- ⁷⁹⁸ A. T. I. Adamou and R. V. Craster, "Spectral methods for modelling guided waves in elastic media," *J. Acoust. Soc. Am.* **116**(3), 1524–1535 (2004).
- ⁷⁹⁹ F. Karpfinger, B. Gurevich, and A. Bakulin, "Modeling of wave dispersion along cylindrical structures using the spectral method," *J. Acoust. Soc. Am.* **124**(2), 859–865 (2008).
- ⁸⁰⁰ F. H. Quintanilla, M. J. S. Lowe, and R. V. Craster, "Modeling guided elastic waves in generally anisotropic media using a spectral collocation method," *J. Acoust. Soc. Am.* **137**(3), 1180–1194 (2015).
- ⁸⁰¹ A. Hood, "Localizing the eigenvalues of matrix-valued functions: Analysis and applications," Ph.D. thesis (Cornell University Library, 2017).
- ⁸⁰² T. Betcke, N. J. Higham, V. Mehrmann, C. Schröder, and F. Tisseur, "NLEVP: A collection of nonlinear eigenvalue problems," *ACM Trans. Math. Softw.* **39**(2), 1–28 (2013).
- ⁸⁰³ I. Gohberg, P. Lancaster, and L. Rodman, *Matrix Polynomials* (Society for Industrial and Applied Mathematics, 2009).
- ⁸⁰⁴ H. Gravenkamp, B. Plestenjak, D. A. Kiefer, and E. Jarlebring, "Computation of leaky waves in layered structures coupled to unbounded media by exploiting multiparameter eigenvalue problems," *arXiv:2404.15277*.
- ⁸⁰⁵ J. A. Weideman and S. C. Reddy, "A MATLAB differentiation matrix suite," *ACM Trans. Math. Softw.* **26**(4), 465–519 (2000).
- ⁸⁰⁶ R. Baltensperger and M. R. Trummer, "Spectral differencing with a twist," *SIAM J. Sci. Comput.* **24**(5), 1465–1487 (2003).
- ⁸⁰⁷ G. Strang, *Introduction to Linear Algebra* (SIAM, 2022).
- ⁸⁰⁸ N. Atalla, R. Panneton, and P. Debergue, "A mixed displacement-pressure formulation for poroelastic materials," *J. Acoust. Soc. Am.* **104**(3), 1444–1452 (1998).
- ⁸⁰⁹ J.-F. Allard and N. Atalla, *Propagation of Sound in Porous Media: Modelling Sound Absorbing Materials*, 2nd ed. (Wiley, Hoboken, NJ, 2009).
- ⁸¹⁰ J. D. Achenbach, H. A. Lauwerier, and W. T. Koiter, *Wave Propagation in Elastic Solids*, North-Holland Series in Applied Mathematics and Mechanics (Elsevier Science, Amsterdam, 2014).
- ⁸¹¹ P. Debergue, R. Panneton, and N. Atalla, "Boundary conditions for the weak formulation of the mixed (u,p) poroelasticity problem," *J. Acoust. Soc. Am.* **106**(5), 2383–2390 (1999).
- ⁸¹² L. Brillouin, *Wave Propagation in Periodic Structures* (MGH, 1946).
- ⁸¹³ A. Bernard, M. J. S. Lowe, and M. Deschamps, "Guided waves energy velocity in absorbing and non-absorbing plates," *J. Acoust. Soc. Am.* **110**(1), 186–196 (2001).
- ⁸¹⁴ F. Simonetti and M. J. S. Lowe, "On the meaning of Lamb mode nonpropagating branches," *J. Acoust. Soc. Am.* **118**(1), 186–192 (2005).
- ⁸¹⁵ M. Castaings and B. Hosten, "Guided waves propagating in sandwich structures made of anisotropic, viscoelastic, composite materials," *J. Acoust. Soc. Am.* **113**(5), 2622–2634 (2003).
- ⁸¹⁶ J. M. Carcione, "Wave propagation in anisotropic, saturated porous media: Plane-wave theory and numerical simulation," *J. Acoust. Soc. Am.* **99**(5), 2655–2666 (1996).
- ⁸¹⁷ A. Geslain, S. Raetz, M. Hiraiwa, M. Abi Ghanem, S. P. Wallen, A. Khanolkar, N. Boechler, J. Laurent, C. Prada, A. Duclos, P. Leclaire, and J.-P. Groby, "Spatial Laplace transform for complex wavenumber recovery and its application to the analysis of attenuation in acoustic systems," *J. Appl. Phys.* **120**(13), 135107 (2016).
- ⁸¹⁸ O. Dazel, F. Sgard, F.-X. Becot, and N. Atalla, "Expressions of dissipated powers and stored energies in poroelastic media modeled by (u,U) and (u,P) formulations," *J. Acoust. Soc. Am.* **123**(4), 2054 (2008).
- ⁸¹⁹ D. Royer and T. Valier-Brasier, *Ondes élastiques Dans les Solides*, Collection Ondes, ISTE éditions (ISTE, London, 2021).